Journal of Catalysis 266 (2009) 308–319

Contents lists available at ScienceDirect

Journal of Catalysis

journal homepage: www.elsevier.com/locate/jcat

Study of active sites and mechanism responsible for highly selective CO oxidation in H_2 rich atmospheres on a mixed Cu and Ce oxide catalyst

Christopher S. Polster, Hari Nair, Chelsey D. Baertsch *

School of Chemical Engineering, Purdue University, 480 Stadium Mall Drive, West Lafayette, IN 47907, USA

ARTICLE INFO

Article history:
Received 4 May 2009
Revised 20 June 2009
Accepted 23 June 2009
Available online 28 July 2009

Keywords:
Copper
Ceria
Mixed oxide
Active site density
Anaerobic reaction
Anaerobic titration
PROX
CO oxidation
H_2 oxidation
Redox mechanism

ABSTRACT

Preferential oxidation of CO in H_2 was studied over a series of CuO_x–CeO_2 mixed oxide catalysts with differing Cu loadings and preparation techniques to elucidate structure and mechanism parameters required to achieve high selectivity. Using *in situ* diffuse reflectance infra-red Fourier transform spectroscopy (DRIFTS), CO oxidation activity is linked to Cu^+ carbonyl species (~2110 cm^{-1}), while catalyst deactivation is associated with catalyst hydration. Active sites for both reactions are found to be reducible oxygen from highly dispersed or surface incorporated CuO_x species in proximity to Ce, and are quantified utilizing anaerobic titrations. Active site concentrations (2.1–3.5 × 10^{-6} mol O^* m^{-2}) are correlated with surface copper content, as determined by X-ray photoelectron spectroscopy (XPS). High reaction selectivity towards CO oxidation (100% selectivity above 200 ppm CO at 333 K) is attributed to preferential adsorption of CO as well as inhibited H_2 dissociation due to oxidized copper sites. A detailed Mars and van Krevelen mechanism for CO and H_2 oxidation is proposed and supported by comparing the model to the experimental data.

1. Introduction

CuO_x–CeO_2 catalysts are known for their high selectivity for CO oxidation in atmospheres with excess H_2, for applications both in CO preferential oxidation (PROX) systems (CO concentration ~1%) [1–15] and in reactive CO sensors (CO concentration ~100 ppm) [16]. In many of these works, rate expressions are proposed and fit to data and some mechanistic steps are proposed, but no work includes a full mechanism for both CO and H_2 oxidation pathways. Previously, it was suggested that the high PROX selectivity of CuO_x–CeO_2 catalysts is partially due to competitive adsorption effects between CO and H_2 [16]. Also suggested in this work was that inherent differences between CO and H_2 oxidation kinetics also contribute to the high selectivity. A goal of this study is to elucidate the reaction pathways, and to use this new understanding of the mechanism to discuss factors which lead to high selectivity.

It is commonly accepted for CuO_x–CeO_2 catalysts that oxidation pathways are facilitated by a form of mobile oxygen [5,7,12,17]. Generally the mobile oxygen is attributed to interfacial sites between CuO_x and CeO_2 domains. Comparative investigations of CuO_x–CeO_2 catalysts prepared by both incipient wetness impregnation and a reverse microemulsion method show that Cu domains with higher dispersion have a higher activity towards CO oxidation and that high copper loadings lead to a decrease in CO oxidation selectivity with respect to H_2 oxidation [5]. Progressive Ar^+ sputtering XPS also showed that the reverse microemulsion technique is more effective at segregating Cu than incipient wetness, in the form of either copper oxides or copper-enriched Cu–Ce mixed oxides. The formation of a mixed oxide phase is possible as a substitution solid solution considering the ionic radii of Ce^{+4} (0.111 nm) and Cu^+ (0.115 nm) [12,17]. Increased activity (for both CO and H_2 oxidation) of these segregated Cu species is correlated to the ease of reduction (or oxygen vacancy formation); an idea supported by other studies [7,12]. Though the requirement of active lattice oxygen is a common idea among many works, no active lattice site densities have been reported. Such redox site densities are important for the determination of intrinsic activity and accurate comparison of rates over $CuCeO_x$ catalysts with variable preparation, Cu content and dispersion [18,19]. Therefore, another main purpose of this work is to measure the quantity of active oxygen sites on CuO_x–CeO_2 catalysts with variable Cu content and surface dispersion and relate it to both activity and the level of incorporation between Cu and CeO_2.

* Corresponding author. Fax: +1 765 494 0805.
E-mail address: baertsch@purdue.edu (C.D. Baertsch).

0021-9517/$ - see front matter © 2009 Elsevier Inc. All rights reserved.
doi:10.1016/j.jcat.2009.06.021

2. Experimental

2.1. Catalyst synthesis

In an attempt to achieve a high degree of mixing between CuO and CeO_2 phases and to compare influences of the degree of Cu dispersion on rates and selectivity amongst catalyst samples, CuO_x–CeO_2 catalysts were synthesized by both the urea gelation technique [7] and co-precipitation [2]. $Cu(NO_3)_2{\cdot}3H_2O$ (Alfa Aesar, ACS reagent) and $(NH_4)_2Ce(NO_3)_6$ (Alfa Aesar, 99.5%) precursors were used in both cases. For urea gelation catalysts, precursors were dissolved in 135 mL deionized water to a total molarity of approximately 0.5 M with relative proportions to contain 10 atom% Cu. A 7.5 M solution of urea (Alfa Aesar, 99.5%) one-third of the volume of the precursor solution was also prepared. Both solutions were heated to near their boiling points and the urea solution was added steadily by a buret to the precursor solution over a period of 0.167 h (a total of 45.5 mL) while stirring. The solution was then stirred and boiled gently (around 373 K) for 2 h during which the solution became a gel and changed its color from bright orange to dark green, after which it was aged for another 2.5 h at approximately 415 K. The aged material was washed twice by stirring vigorously in hot deionized water for 0.5 h and then vacuum filtered. The catalysts were dried overnight in an oven at 383 K and calcined in dry air at 923 K for 4 h.

For the preparation of co-precipitated CuO_x–CeO_2, 50 mL of 0.15 M $Cu(NO_3)_2{\cdot}3H_2O$ and 500 mL of 0.075 M $(NH_4)_2Ce(NO_3)_6$ were mixed together at room temperature and precipitated by the fixed rate addition of 7% w/v Na_2CO_3 (Fisher Scientific) over 1.33 h (a total volume of 118 mL). The precipitated mixture was stirred for an additional 0.5 h, then filtered, washed, dried and calcined as described above.

The catalysts used in this study are referred to as $CuCeO_x$–UG x.x or $CuCeO_x$–CP x.x where UG and CP, respectively, stand for urea gelation and co-precipitation, and x.x is the atomic percentage of Cu determined by atomic absorption spectrometry (AAS). A pure CeO_2 sample is also prepared by urea gelation, referred to as CeO_2–UG.

2.2. Catalyst structure characterization

The CuO_x–CeO_2 catalysts were characterized by X-ray diffraction (XRD), X-ray photoelectron spectroscopy (XPS), high resolution transmission electron microscopy (HR-TEM), atomic absorption spectrometry (AAS) and temperature-programmed reduction (TPR). XRD patterns were collected using a Scintag X2 diffractometer using Cu Kα radiation (wavelength = 0.1541 nm) and a scanning rate of 1.2°/min. The Scherrer formula [20] was used to calculate catalyst crystallite size. This value was calculated for five of the principal diffraction peaks for fluorite CeO_2 [(111), (200), (220), (311) and (222)] and the average value is reported. XPS spectra of powdered samples were collected using a Kratos AXIS spectrometer fitted with a charge neutralizer. Survey spectra were completed using a pass energy of 160 eV and a dwell time of 0.8 s, while narrow region spectra for Cu 2p and Ce 3d were done with a pass energy of 20 eV and a dwell time of 0.2 s. Region spectra are a result of averaging at least four scans over the region. CasaXPS version 2.3.12, using built in relative sensitivity factors for Cu $2p_{3/2}$ and Ce $3d_{5/2}$ peaks, was used to quantify relative Cu:Ce surface concentrations. For XPS measurement, powdered catalyst was spread onto double-sided conductive tape and placed on the sample holder. Two spectra were collected for each sample at different positions on the powdered catalyst film to ensure sample homogeneity, and average results are reported.

Transmission Electron Micrographs were collected on a FEI Titan 80 field-emission Environmental Cell Transmission Electron Microscope/Scanning Transmission Electron Microscope (E-TEM/STEM) at an operating voltage of 300 kV. Electron energy loss spectra were collected using a Gatan Image Filter. Images were collected at low magnification to ensure uniformity of the surface and high magnification images are shown as representative of the surface. Electron Energy Loss Spectroscopy (EELS) was performed by switching from imaging to spectroscopy mode and collecting data over the same region as imaged. Ground solid catalysts were deposited on a holey carbon grid (Electron Microscopy Sciences).

Samples for AAS measurements were made by dissolving catalysts in concentrated HNO_3:HCl mixtures (1:3) at ~353 K and then diluting in DI water. Samples were matrix-matched to avoid any potential interference from nitrate or chloride ions. Cu standards of 1, 5 and 10 mg/L were prepared from a 1000 mg/L standard solution (Ricca Chemical). Weight percentages were obtained from concentration measurements (wavelength 324.8 nm, slit 0.7 nm) and atomic percentages were calculated using the stoichiometry $Cu_xCe_{1-x}O_{2-x}$. TPR studies were carried out in a U-shaped quartz reactor (10 mm I.D.). For all TPR experiments, catalysts were reduced using 20 mole% H_2 in Ar (50 sccm, 0.333 K s^{-1}). The reactor effluent was analyzed by mass spectrometry (Hiden HPR 20 Gas Analyzer); monitoring $m/e = 2$ for the consumption of H_2. Catalyst surface areas were determined by nitrogen physisorption (BET method) at 77 K using a Micromeritics ASAP 2000 porosimeter.

All error values reported in this work are calculated assuming that the experimental results are normally distributed. Due to relatively small data sets for most error determination (<10 samples), a *T*-distribution was used to calculate confidence intervals, and in all cases, data are reported to 90% confidence. Errors obtained on quantities determined by linear fits (BET surface area, reaction orders, etc.) are based on standard error of the slope parameter, and are also given as 90% confidence intervals as described. Errors on calculated quantities (normalized rates, surface densities, etc.) are calculated using appropriate error propagation for the equations used.

2.3. Reaction characterization

Two different sets of conditions with significantly different CO pressures were used to investigate the rate, selectivity and mechanism for selective CO oxidation in H_2 over CuO_x–CeO_2 catalysts. Conditions typical of many PROX studies [3,11,21] were used for benchmarking purposes. For these conditions, reactions were carried out at 313–413 K in 50% H_2, 1% CO, 0.5% O_2 and balance He. Conditions relevant for gas sensor applications were also investigated in this study. For these conditions [16], reactions were carried out at 333–353 K in excess H_2 (typically 25–50%) with varying CO and O_2 concentrations between 50 and 5000 ppm. Catalyst powders (particle sizes 75–125 μm) were supported on a quartz frit in a vertical U-shaped quartz reactor (I.D. 10 mm). Temperature measurement and control was performed with a thermocouple resting in a well in contact with the catalyst bed. Reactor effluent was analyzed using an Agilent MicroGC 3000, with a lower detection limit on water of approximately 2 ppm. Fractional conversions for both CO and H_2 were calculated by disappearance, shown by example in (1), where $P_{CO,out}$ is the CO partial pressure in the product mixture under reaction conditions and $P_{CO,in}$ is the CO partial pressure in the reaction feed. Reaction selectivity was calculated by product formation, shown by (2), where $P_{CO_2,out}$ and $P_{H_2O,out}$ are CO_2 and H_2O partial pressures under reaction conditions. No other products were observed at any tested reaction conditions.

$$X_{CO} = 1 - P_{CO,out}/P_{CO,in} \quad (1)$$

$$S_{CO_2} = P_{CO_2,out}/(P_{CO_2,out} + P_{H_2O,out}) \times 100\% \quad (2)$$

All rate measurements were made after first treating the catalyst in 10% O_2 balance He for 0.5 h at 773 K, then subjecting the catalyst to reaction conditions for 12–16 h. After an initial deactivation period (~12 h), the catalyst activity was very stable over long time frames (>50 h). A similar pretreatment method has been previously developed [12].

Anaerobic titrations, an experiment detailed in another work [19], were used as a method to quantify redox site densities for catalysts in this study. In this method, O_2 is instantaneously removed from a steady-state oxidation process and replaced with a make-up flow of He using a 4-port zero dead volume Valco switching valve. The reactor system reached zero O_2 concentration within 15 s of the switch time for all experiments in this study, as verified by monitoring $m/z = 32$ using a Hiden HPR 20 Gas Analyzer. Anaerobic titrations were performed using both CO and H_2, either separately or together, as probe molecules. Product formation rates during anaerobic titration were measured by mass spectrometry for CO titrations ($m/z = 44$) and by Micro GC for H_2 and PROX titrations.

2.4. In situ DRIFTS measurements

In situ diffuse reflectance infra-red Fourier transform spectroscopy (DRIFTS) data were collected with a Nicolet Magna-860 spectrometer using a Harrick Scientific Praying Mantis diffuse reflectance accessory (DRA) and *in situ* reaction cell (HVC-DRP). Spectra were averaged over 128 scans with a resolution of 4 cm^{-1} and mirror velocity of 1.8988 cm s^{-1}. Approximately 30 mg of powdered catalyst was loaded into the reaction cell and supported on a horizontal quartz frit. Gases were mixed upstream by Tylan mass flow controllers and passed downward through the catalyst bed. Temperature was measured and controlled by a thermocouple immediately beneath the catalyst bed. The infra-red beam was focused onto the catalyst surface prior to enclosing the catalyst in a dome fitted with ZnS windows. A background spectrum was collected at reaction temperature after pretreatment in 10% O_2 balance He at 773 K. This background spectrum was used to convert reflectance measurements into pseudo-absorbance units using the Kubelka–Munk methodology [22]. DRIFTS was used in this study to monitor surface species during catalyst deactivation in 25% H_2, 1% CO, 3% O_2, and the balance He at 333 K.

3. Results and discussion

3.1. Characterization of catalyst structure

The structure of three prepared CuO_x–CeO_2 catalysts and one pure CeO_2 sample was characterized using complementary techniques; their properties are reported in Table 1. Previously, it was demonstrated that the optimal catalyst structure for high activity and selectivity is a mixed Cu and Ce oxide [3,17]. As shown in Fig. 1, X-ray diffraction peak positions are identical for all catalysts and match what is expected for pure fluorite CeO_2 [23]. The absence of Cu, Cu_2O and CuO peaks as determined by XRD is consistent with a high level of Cu incorporation within CeO_2. Although unmixed copper oxide species may still exist on the surface, such domains are either too small or not crystalline enough to be observed by XRD and thus a significant portion of the Cu must be in proximity to Ce. The Cu is also possibly incorporated in a substitution solid solution with CeO_2 as noted in other studies [12,17]. The distinguishably sharper peaks for pure CeO_2 indicate larger crystallite size than the CuO_x–CeO_2 samples, as quantified in Table 1. The shorter range crystallinity of the CuO_x–CeO_2 samples can possibly be attributed to the presence of Cu interrupting crystallization during synthesis, or perhaps disrupting CeO_2 annealing during calcination.

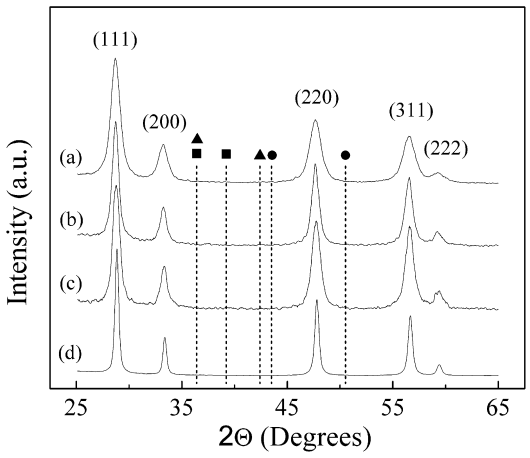

Fig. 1. Powder X-ray diffraction patterns for (a) $CuCeO_x$–UG 4.0, (b) $CuCeO_x$–CP 9.1, (c) $CuCeO_x$–UG 2.5 and (d) CeO_2–UG. All XRD patterns are normalized by (111) peak intensity. Dotted lines show expected peak positions for (■) CuO [3], (▲) Cu_2O [34] and (●) Cu [35].

High Resolution Transmission Electron Microscopy (HR-TEM) and Electron Energy Loss Spectroscopy (EELS) were also used to probe the dispersion of Cu in the CuO_x–CeO_2 catalysts. Fig. 2a shows a representative Transmission Electron Micrograph collected over the $CuCeO_x$–UG 4.0 catalyst. No domains of CuO_x are visible – structural characteristics resemble those of ceria alone (images not shown here). This was further confirmed by EELS data collected over the same catalyst (Fig. 2b). The spectrum shows an adsorption edge at 883 eV with two peaks separated by about 15 eV, corresponding to the M5 and M4 absorption edges of Ce in CeO_2 [24]. Micrographs and EELS data collected over the $CuCeO_x$–UG 2.5 and the $CuCeO_x$–CP 9.1 catalysts showed similar features, suggesting that extremely small amounts of Cu are present in these catalysts and almost none of it is present as surface CuO_x. To test the efficacy of TEM and EELS in detecting bulk CuO_x in these catalysts, another catalyst was prepared by the same method as $CuCeO_x$–UG 4.0, but calcined at ~1123 K. It is known that a higher calcination temperature results in Cu segregation from the lattice and hence more CuO_x formed on the CeO_2 surface [6]. A TEM

Table 1
Summary of catalyst structure properties.

Catalyst name[a]	Copper content (wt%)[b]	BET surface area ($m^2\ g^{-1}$)	XRD crystallite size (nm)[c]	XPS surface Cu:Ce ratio[d]
CeO_2–UG	–	16.0 ± 0.1	22 ± 3	–
$CuCeO_x$–UG 2.5	0.8 ± 0.2	36.3 ± 0.2	11 ± 3	0.36 ± 0.04
$CuCeO_x$–UG 4.0	1.3 ± 0.2	115.8 ± 0.7	8 ± 2	0.17 ± 0.02
$CuCeO_x$–CP 9.1	3.0 ± 0.1	57.8 ± 0.4	12 ± 3	0.49 ± 0.07

[a] UG and CP represent urea gelation and co-precipitation, respectively. Number represents Cu content in atomic percentage.
[b] Copper content determined by AAS.
[c] Crystallite sizes calculated from the Scherrer formula [20].
[d] Surface ratios (Cu:Ce) calculated from peak areas of Cu $2p_{1/2}$ and Ce $3d_{5/2}$, using built in relative sensitivity factors in CasaXPS version 2.3.12.

micrograph of this catalyst is shown in Fig. 2c and shows highly crystalline particles with dark patches of observed CuO_x. EELS spectra collected over this catalyst (Fig. 2d) show that in addition to the absorption edges associated with Ce (883 eV and 901 eV), absorption associated with the Cu L2 and L3 edges are also seen at ~925 eV and 945 [24]. The contrasting results suggest that most surface Cu species in the $CuCeO_x$–UG 2.5 and the $CuCeO_x$–CP 9.1 catalysts are in the form of Cu–O–Ce, rather than as crystalline CuO. However, differentiation between Cu–O–Ce species containing Cu substituted into the CeO_2 lattice with very small amorphous CuO_x monolayers/submonolayers on the CeO_2 surface is not possible from these TEM results.

Fresh catalysts were characterized by *ex situ* XPS to determine relative surface concentrations of Cu and to observe the average oxidation state of Cu and Ce in prepared samples. Relative Cu:Ce surface concentrations, when compared to the bulk atomic Cu concentration, can be used as a measure of Cu incorporation. The closer the surface concentration is to the bulk concentration, the higher degree of Cu incorporation. Survey scans were used to calculate the Cu:Ce ratios reported in Table 1. The bulk Cu to bulk Ce atomic ratios are 0.026, 0.042 and 0.100 for $CuCeO_x$–UG 2.5, $CuCeO_x$–UG 4.0 and $CuCeO_x$–CP 9.1, respectively. The surface ratios of $CuCeO_x$–UG 4.0 and $CuCeO_x$–CP 9.1 are only 4 and 5 times the value of their respective bulk ratios, compared to 14 times for the $CuCeO_x$–UG 2.5 catalyst, suggesting that Cu in the $CuCeO_x$–UG 2.5 catalyst is more segregated to the surface (less incorporated into the bulk) than the other catalysts, though all catalysts seem to exhibit significant segregation of Cu to the surface.

Figs. 3 and 4 show the Cu 2p and Ce 3d XPS regions. The spectra are normalized by their peak intensity and energy corrected for adventitious carbon at 284.0 eV. From Fig. 3, it is apparent that most Cu initially present in these samples is in a +1 oxidation state due to the absence of shake-up peaks that are expected for Cu^{2+} at 939–944 eV [3]. However, some of the Cu in the $CuCeO_x$–CP 9.1 catalyst appears to be in a +2 oxidation state, as both the $2p_{3/2}$ and $2p_{1/2}$ peaks are noticeably broadening to higher binding energies. The Ce 3d XPS of $CuCeO_x$–CP 9.1 also differs noticeably from the UG catalysts (Fig. 4). While the Ce in both $CuCeO_x$–UG samples seems to be mostly in a +4 oxidation state, the $CuCeO_x$–CP 9.1 sample contains more Ce^{3+} character due to the reduction of peaks at 880.9 and 896.8 eV and the appearance of a feature around 883 eV, where Ce^{3+} is expected [25]. These observations together are indicative of the redox equilibrium ($Cu^{1+} + Ce^{4+} \leftrightarrow Cu^{2+} + Ce^{3+}$) [8,12] which is shifted to the right in the $CuCeO_x$–CP 9.1 catalyst relative to the UG catalysts.

This equilibrium has been claimed to be the source of a synergetic effect on catalyst reducibility [12] which is evidenced by temperature- programmed reduction (TPR) experiments. Fig. 5

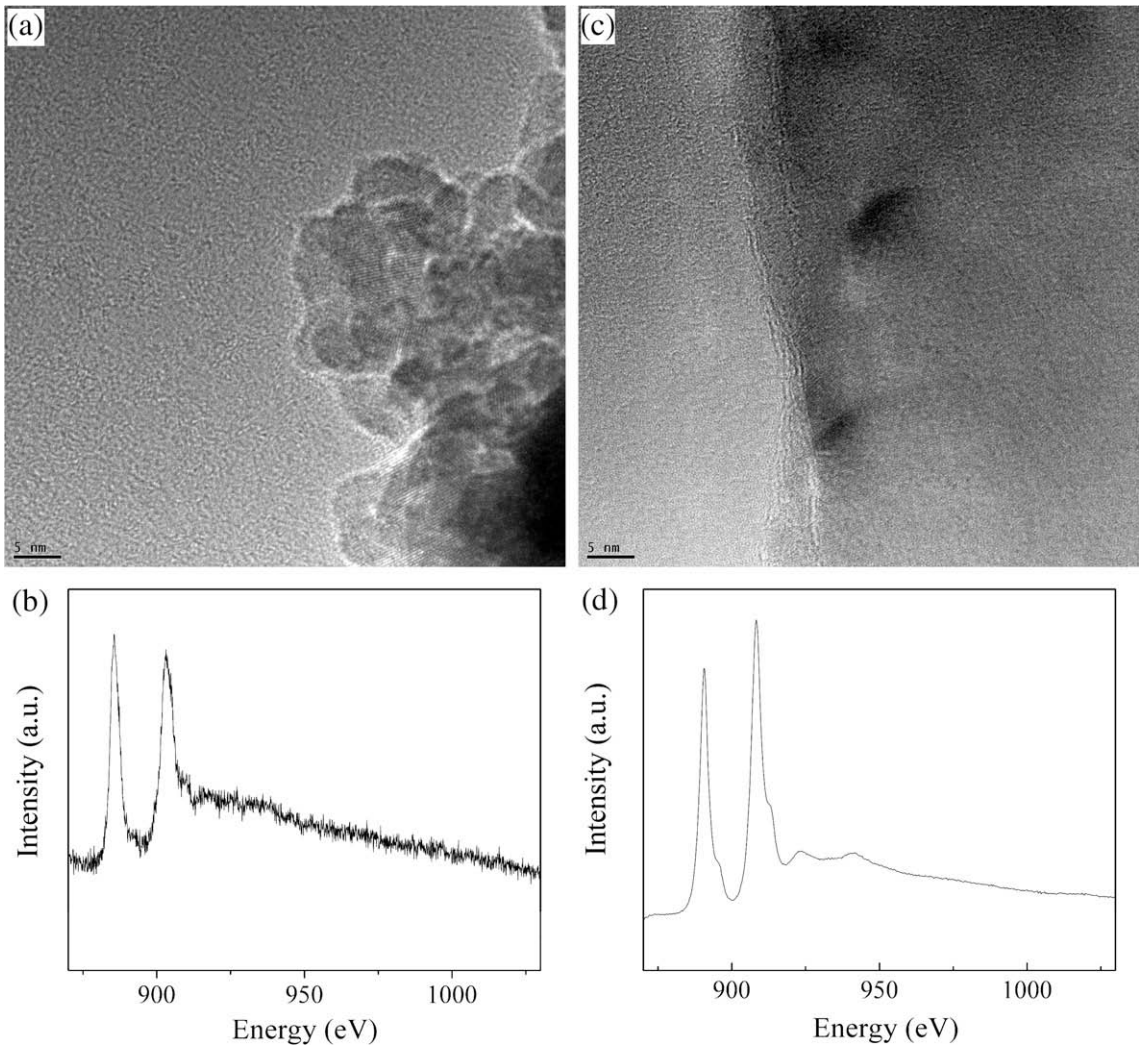

Fig. 2. HR-TEM images of (a) $CuCeO_x$–UG 4.0 and (c) $CuCeO_x$–UG calcined at 1123 K with the corresponding EELS spectra of (b) $CuCeO_x$–UG 4.0 and (d) $CuCeO_x$–UG calcined at 1123 K.

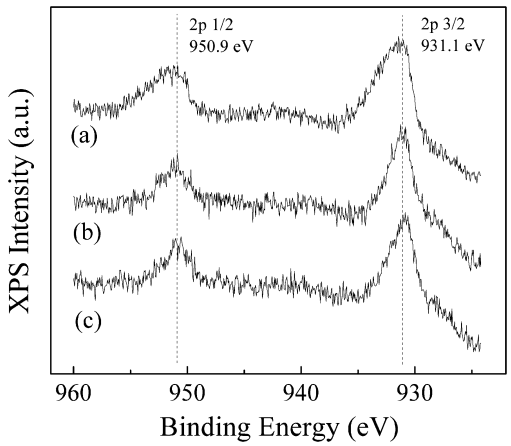

Fig. 3. XPS region spectra of (a) $CuCeO_x$–CP 9.1, (b) $CuCeO_x$–UG 4.0 and (c) $CuCeO_x$–UG 2.5 over the Cu 2p region.

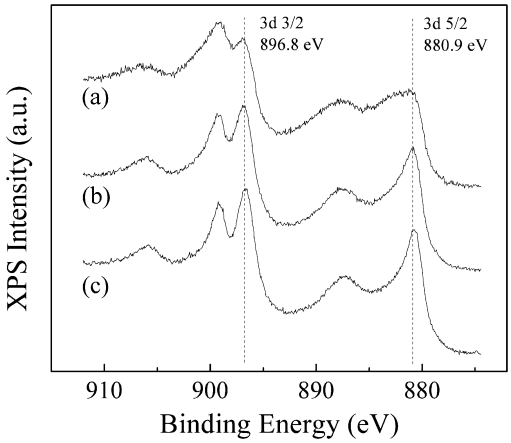

Fig. 4. XPS region spectra of (a) $CuCeO_x$–CP 9.1, (b) $CuCeO_x$–UG 4.0 and (c) $CuCeO_x$–UG 2.5 over the Ce 3d region.

compares the H_2–TPR results for CuO, Cu_2O and the three prepared $CuCeO_x$ catalysts. TPR data for CeO_2 are not included here, but CeO_2 is known to have two reduction peaks at 773 and 1073 K [26]. CuO_x–CeO_2 reduces at a considerably lower temperature (peaks at 414 and 453 K) than CuO (574 K), Cu_2O (621 K) or CeO_2, which suggests that the oxygen species being reduced in CuO_x–CeO_2 must not resemble oxygen species in either of the pure oxides. TPR experiments with CO show a similar reduction in CuO_x–CeO_2 reduction peak temperatures, and have been shown to agree with catalyst activity data [27].

The two-peak H_2–TPR profile of CuO_x–CeO_2 is consistent with a phenomenon discussed in detail in Section 3.3 and elsewhere [28] regarding the generation of sites for facile H_2 dissociation. Once copper oxides are reduced to a certain extent, they tend to dissociate H_2 much easier and then reduce at higher rates, which is one potential source of the 453 K TPR peak. Table 2 compares TPR peak area ratios (ratio of the lower temperature TPR peak to the higher temperature TPR peak) with the degree of Cu segregation (Cu:Ce surface ratio divided by Cu:Ce bulk ratio). A higher degree of Cu segregation from bulk (lower surface dispersion of Cu) correlates with a lower peak ratio, suggesting that catalysts with higher Cu dispersion (more Ce–O–Cu sites) will resist facile H_2 dissociation to a higher degree of reduction. It follows that the reduction of Cu–O–Cu sites in close contact with CeO_2 (not resembling pure CuO) create sites on which H_2 can be dissociated much easier. This also supports the idea that the redox capabilities of this catalyst are a result of small amorphous CuO_x domains in close contact with CeO_2 or direct incorporation of Cu into the CeO_2 lattice.

3.2. Catalyst deactivation and activity comparison

After 0.5 h of pretreatment in 10% O_2 balance He at 773 K, all the catalysts in this study deactivate over a period of several hours. Fig. 6 shows an example of CO oxidation deactivation over $CuCeO_x$–CP 9.1 in H_2 excess. The majority of the deactivation is complete within approximately 4 h (deactivation time constant 0.6 h^{-1}), after which the rate is mostly stable. The nature of this deactivation is described by diffuse reflectance

Table 2
Comparison of Cu surface segregation and TPR peak ratios.

Catalyst name	Degree of Cu segregation[a]	Peak area ratio[b] (A_{LT}/A_{HT})
$CuCeO_x$–UG 4.0	4	0.33
$CuCeO_x$–CP 9.1	5	0.26
$CuCeO_x$–UG 2.5	14	0.16

[a] Degree of Cu segregation refers to a ratio of Cu surface concentration (measured by XPS) to Cu bulk concentration (measured by AAS).
[b] Peak area ratio refers to the ratio of the two H_2–TPR peaks at low and high temperatures, respectively.

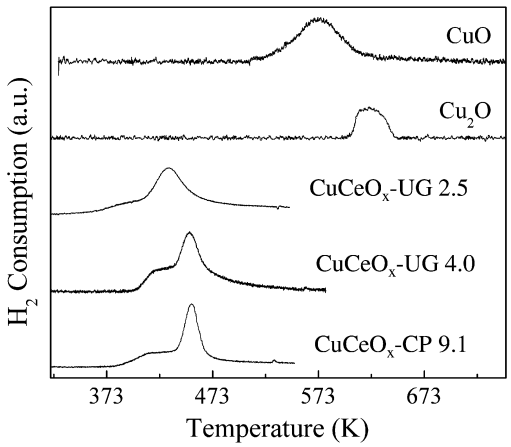

Fig. 5. H_2-TPR results for CuO, Cu_2O and $CuCeO_x$ catalysts. Results are normalized by catalyst Cu content.

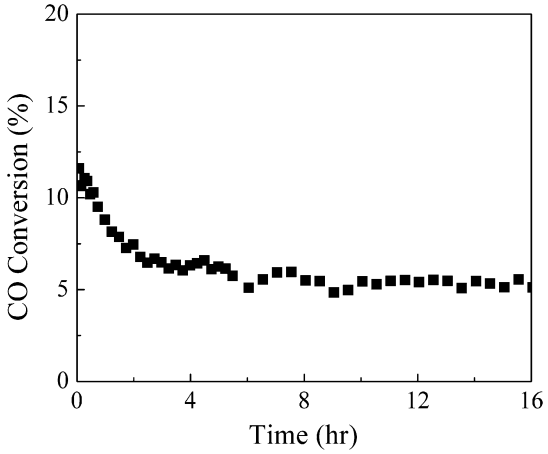

Fig. 6. Deactivation of $CuCeO_x$–CP 9.1. Reaction conditions: 50% H_2, 2% CO, 1% O_2, bal He. Flow rate = 100 sccm, catalyst weight = 150 mg, temperature = 323 K.

infra-red Fourier transform spectroscopy (DRIFTS) studies presented in Section 3.4.

Fig. 7 shows the characteristic PROX performance of the three CuO_x–CeO_2 catalysts studied in 50% H_2, 1% CO, 0.5% O_2, and the balance He (100 mg catalyst, 100 sccm). Under these conditions, there is no distinguishable difference in selectivity between the three catalysts. However, there are noticeable differences in the CO oxidation rates. The difference in rates per gram (at 333 K) between $CuCeO_x$–UG 2.5 (2.1×10^{-7} mol g^{-1} s^{-1}) and $CuCeO_x$–UG 4.0 (6.2×10^{-7} mol g^{-1} s^{-1}) apparently result in part from their different surface areas, as their surface areas differ by a factor of ~3. The rate per surface area of $CuCeO_x$–CP 9.1 (1.2×10^{-8} mol m^{-2} s^{-1}), however, is higher than either UG catalyst (~5.4×10^{-9} mol m^{-2} s^{-1}), suggesting that the CP catalyst has a higher density of active redox sites and emphasizing on the fact that better rate normalization techniques are necessary to compare turnover frequencies (one goal of this work). The CP catalyst has a higher concentration of Cu at the surface than either UG catalyst (Table 1), but the Cu:Ce surface ratio does not fully describe the differences in catalyst activity. It therefore is necessary to identify and quantify the active redox sites in these catalysts to understand the functions responsible for their apparent differing activity.

3.3. Turnover rate comparisons

To rigorously compare the performance and function of the prepared CuO_x–CeO_2 catalysts and structure-dependence on rates for selective CO oxidation, turnover frequencies were compared. For this, the number of active redox sites was determined using anaerobic titrations. Anaerobic titrations have been shown by Nair et al. to accurately quantify active site densities on redox catalysts for use in calculating turnover frequencies [19]. In this technique, gas phase oxygen is removed instantaneously from the reactant stream during steady-state reaction. The formation of oxidation products after the gaseous oxygen removal is attributed to the use of oxygen in the catalyst structure. These removable oxygen atoms are considered to be the active and available surface redox sites and their number can be used to quantify active site densities and oxidation turnover frequencies. Fig. 8a shows the response of $m/z = 44$ as O_2 is removed from the steady-state reaction of 1% CO and 0.5% O_2 at 333 K over $CuCeO_x$–CP 9.1. The fact that the CO oxidation rate decays over ~1 h suggests that the mechanism involves either chemisorbed oxygen (Langmuir–Hinshelwood mechanism) or the extraction of lattice oxygen (Mars and van Krevelen mechanism) as opposed to utilization of gas phase oxygen (Eley–Rideal mechanism) as the active intermediate. Integration beneath the decay curve provides a measure of the lattice oxygen consumed in the transient experiment. The amount of oxygen measured by anaerobic titration is greater than the amounts expected for either physisorbed or chemisorbed oxygen, which confirms that lattice oxygen must be involved in oxidation processes [12].

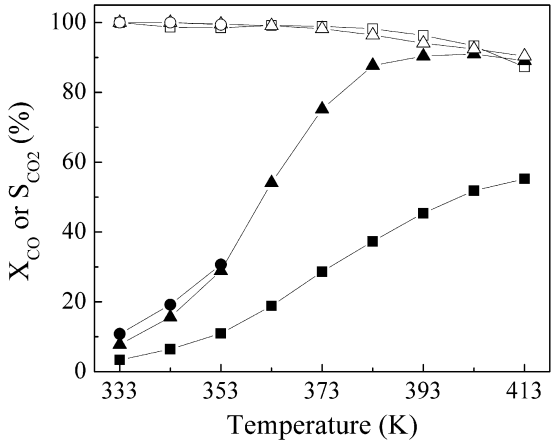

Fig. 7. CO conversion (closed shapes) and CO_2 selectivity (open shapes) as a function of temperature for (■) $CuCeO_x$–UG 2.5, (▲) $CuCeO_x$–UG 4.0 and (●) $CuCeO_x$–CP 9.1. Reaction conditions: 50% H_2, 1% CO, 0.5% O_2, bal He. Flow rate = 100 sccm, catalyst weight = 100 mg.

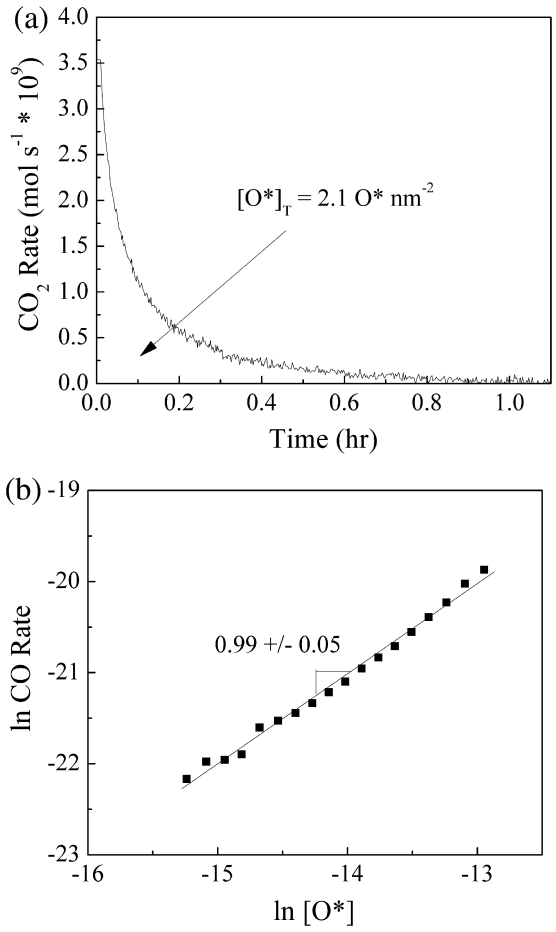

Fig. 8. (a) Response of CO oxidation rate over $CuCeO_x$–CP 9.1 to the removal of oxygen. Initial conditions: 1% CO, 0.5% O_2, balance He at 333 K. Oxygen is replaced with He make-up at $t = 0$. Total flow = 50 sccm. Catalyst weight = 25 mg. (b) Log–log plot of CO oxidation rate vs. remaining O^* concentration.

CO oxidation rates follow a first-order decay with respect to remaining oxygen content (Fig. 8b); thus, the rate-determining step for CO oxidation on CuO_x–CeO_2 must involve only one lattice oxygen atom. Table 3 shows measured active oxygen site densities and turnover frequencies per redox site for the three CuO_x–CeO_2 catalysts studied. The TOF for CO oxidation is indistinguishable within error (*T*-tests performed at 90% confidence) for all CuO_x–CeO_2 catalysts characterized. The observed catalyst response during anaerobic reaction and the resulting TOF measurements

Table 3
Comparison of measured active oxygen site density and normalized CO oxidation rates. Steady-state CO oxidation rates measured in 1% CO, 0.5% O_2 balance He at 333 K. Rates are normalized by active oxygen site density $[O^*]_T$.

Catalyst name	$[O^*]_T$ (O^* nm^{-2})	CO oxidation rate (mol [mol O^*]$^{-1}$ s^{-1}) × 10^3
$CuCeO_x$–UG 2.5	1.7 ± 0.1	2.1 ± 0.2
$CuCeO_x$–UG 4.0	1.3 ± 0.2	2.6 ± 0.5
$CuCeO_x$–CP 9.1	2.1 ± 0.2	2.1 ± 0.3

lead to several conclusions: (1) the catalysts undergo a reduction step in order to oxidize CO, (2) O_2 is needed to reoxidize active sites to maintain a steady rate and (3) anaerobic titrations lead to an accurate measure of these active oxygen sites on CuO_x–CeO_2. Conclusions 1 and 2 are consistent with previous work on CuO_x–CeO_2 suggesting that a Mars and van Krevelen mechanism is responsible for oxidation reactions [12,15].

Anaerobic titrations were also performed using H_2 or a mixture of CO and H_2 as the probe molecule(s) with a Micro GC to monitor oxidation products (CO_2 and H_2O). Redox site densities quantified with H_2 oxidation (by integration over the entire experiment) are the same as those determined with CO oxidation. Table 4 shows the measured site density for seven different experiments conducted over $CuCeO_x$–UG 4.0. Regardless of the CO/H_2 feed gas concentration, the measured redox site density is consistently 1.3 ± 0.2 O^* per nm^2. Fig. 9 shows the H_2 oxidation rate during anaerobic titrations, with and without 100 ppm CO, as a function of oxygen removal (O^*-atoms removed per nm^2). Before 0.25 O^* per nm^2 are removed, the rate decreases with decreasing catalyst oxygen content in a first-order fashion, as also observed for CO anaerobic titrations; however, a new phenomenon arises during H_2 titrations. Regardless of the presence or absence of CO, the H_2 rate begins to increase at the same point despite the continuing loss of redox-active O^* sites. This phenomenon is consistent with the previous studies using *in situ* XRD to monitor copper oxide reduction by H_2 [28]. A slow reduction of the oxide surface (CuO or Cu_2O) was observed until sites that more readily dissociated H_2 were created. Once such sites were created, reduction of the material was facile. Results in Fig. 9 are consistent with two reduction regimes. First, active surface O^* sites are titrated, resulting in a decrease in H_2 oxidation rates, then at a particular level of reduction (~0.25 O^* consumed per nm^2) the catalyst begins to reduce much more rapidly due to the creation of reduced sites which more easily dissociate H_2. This leads to the conclusion that H_2 dissociation is a necessary step in the catalytic mechanism for H_2 oxidation. However, as the rate decay is first-order with respect to remaining O^* species before dissociation site creation, the rate-determining step for H_2 oxidation must still involve lattice oxygen, and cannot be H_2 dissociation. Rather, the rate-determining step must involve both dissociated H_2 and a lattice oxygen. The increase in H_2 rates with creation of dissociation sites is simply a result of a higher concentration of dissociated H_2 species (increased equilibrium constant for H_2 dissociation). This suggests that the high selectivity characteristic of CuO_x–CeO_2 catalysts can be partially explained by inhibited H_2 dissociation.

Fig. 10 demonstrates this principle during an anaerobic titration on $CuCeO_x$–UG 4.0 with both 50% H_2 and 100 ppm CO. CO oxidation TOF, H_2 oxidation TOF and CO_2 selectivity are shown as a function of O^* removed per nm^2. Before H_2 dissociation sites are created (<0.25 O^* nm^{-2}), the selectivity is high (~93%) and constant; however, once H_2 dissociation sites begin to form, selectivity declines steadily as more sites are generated. This suggests that sufficiently oxidized adsorption sites are resistant to H_2 dissociation, and is consistent with XANES studies that suggest H_2 oxidation requires reduced forms of Cu [4].

Table 4
Comparison of anaerobic titration results for different conditions on $CuCeO_x$–UG 4.0.

Reaction conditions[a]	$[O^*]_T$ (O^* nm^{-2})
1% CO	1.2
1% CO (repeat)	1.1
25% H_2	1.1
50% H_2	1.4
50% H_2 (repeat)	1.4
50% H_2, 1% CO	1.3
50% H_2, 100 ppm CO	1.2

[a] Initial oxygen concentration (before removal) is 0.5% for all experiments

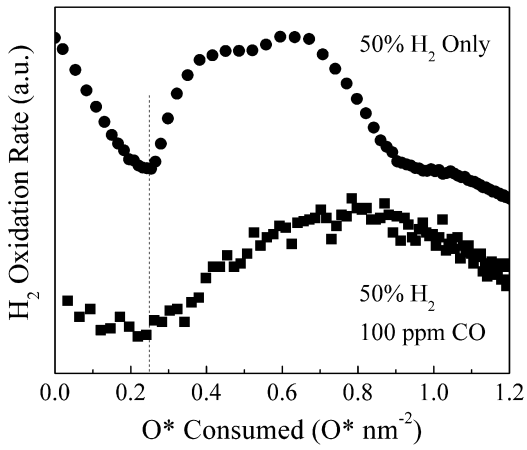

Fig. 9. Two anaerobic titrations of $CuCeO_x$–UG 4.0 at 333 K. Reaction conditions are shown, with balance He.

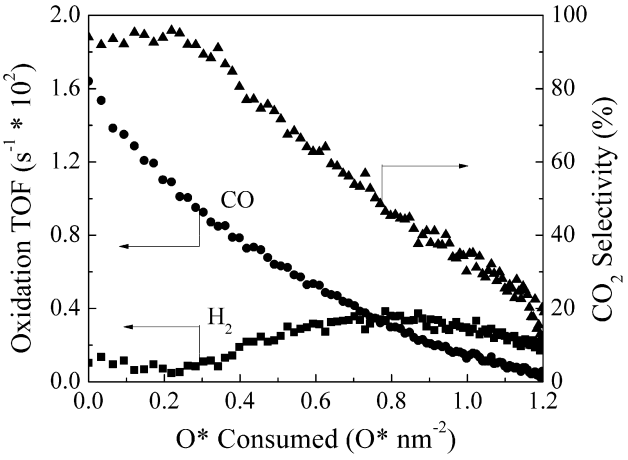

Fig. 10. CO, H_2 oxidation rates and CO_2 selectivity as a function of O^* consumed during the anaerobic titration of $CuCeO_x$–UG 4.0.

In Section 3.1 it is suggested that the active oxygen species are associated with Cu that is closely associated with Ce. XRD shows no bulk crystalline Cu species, so most Cu-atoms at the surface of the catalyst must be accessible. If the active oxygen species are associated with surface Cu-atoms, their surface densities should be correlated. Table 5 compares the surface density of Cu (Cu-atoms nm^{-2}) in all three prepared catalysts (calculated by two methods described below) with the density of active redox oxygen (calculated from anaerobic titrations). BA density refers to the Cu surface density calculated as a bulk average surface density. For this calculation, the weight of copper per gram of catalyst determined by AAS is divided by the specific BET surface area of the catalyst. For the purposes of comparison, BA density assumes that all Cu in the catalysts is fully segregated to and dispersed on the surface. XPS density refers to the atomic surface density of Cu as determined by the Cu:Ce ratios reported in Table 1 and assuming the surface is the (1 1 1) face of a CeO_2 crystal (fcc structure with lattice parameter 0.54113 nm [23]). This gives a metal atom packing of ~7.9 M nm^{-2} from which the Cu density can be calculated directly from XPS Cu:Ce ratios.

BA and XPS Cu surface densities are roughly the same for each of the $CuCeO_x$–UG catalysts (2.1 vs. 2.1 and 1.1 vs. 1.2 Cu nm^{-2}), suggesting that the copper is segregated near the surface of the

Table 5
Comparison of two different copper surface densities to O^* density.

Catalyst name	BA density[a] (Cu nm^{-2})	XPS density[b] (Cu nm^{-2})	O^* density[c] (O^* nm^{-2})
$CuCeO_x$–UG 2.5	2.1 ± 0.5	2.1 ± 0.3	1.7 ± 0.1
$CuCeO_x$–UG 4.0	1.1 ± 0.2	1.2 ± 0.2	1.2 ± 0.2
$CuCeO_x$–CP 9.1	4.9 ± 0.2	2.6 ± 0.6	2.1 ± 0.2

[a] Copper surface density calculated assuming all copper in the catalyst is at the surface.
[b] Copper surface density calculated from relative surface concentrations as measured by XPS
[c] Density of active oxygen species assuming no subsurface reduction.

UG catalysts, but in a highly dispersed form. In contrast, the BA density of $CuCeO_x$–CP 9.1 is considerably higher than its respective XPS density (4.9 vs. 2.6 Cu nm^{-2}), showing that this catalyst must contain subsurface copper, possibly in bulk solid solution with CeO_2. For the $CuCeO_x$–UG catalysts, the calculated Cu surface density is equal to the measured O^* density, but for the CP catalyst the XPS density (2.6 Cu nm^{-2}) compares more favourably with its O^* density (2.1 Cu nm^{-2}) than the BA density (4.9 Cu nm^{-2}). In fact, there is a direct correlation between the surface density of Cu atoms determined by XPS and the active oxygen species measured by anaerobic titration for all catalysts, confirming that the active oxygen species are related to Cu that is closely related to Ce. This correlation is not expected to hold in the case of catalysts containing crystalline CuO_x species, where large portions of Cu are not closely associated with Ce.

3.4. In situ DRIFTS measurements

After oxidative pretreatment at elevated temperatures, CuO_x–CeO_2 is known to deactivate over a period of several hours [12]. The same phenomenon is evident on all catalysts in this study as shown in Section 3.2. *In situ* diffuse reflectance infra-red Fourier transform spectroscopy (DRIFTS) was used to study surface species during the catalyst deactivation period to help understand causes for the change in activity and selectivity when exposed to CO and H_2. Fig. 11 shows the time evolution of carbonate bands during deactivation of $CuCeO_x$–UG 4.0 in 25% H_2, 1% CO, 3% O_2, balance He at 333 K. Within 0.05 h, two major species form: a carbonate bidentate species (bands at 1575, 1295 and 1026 cm^{-1}, found at 1565, 1298 and 1014 cm^{-1} in [25]), and a bicarbonate species (bands at 1395 and 1217 with a shoulder at 1606 cm^{-1}, found at 1393, 1217 and 1611 cm^{-1} in [25]). The peaks at 1395 and 1217 cm^{-1} were assigned to a bicarbonate species, rather than to a bridged carbonate species with reported peaks at similar positions because of the shoulder present at 1606 cm^{-1}, which is due to a bicarbonate species and decays with time very similarly to the two bands observed at 1395 and 1217 cm^{-1}. Many other species are found in the region 1200–1700 cm^{-1}, including polymeric carbonate species and formates [29,30], which may explain peak broadening with time.

Fig. 12 shows the time evolution of both the Cu^+ carbonyl peak at approximately 2120–2110 cm^{-1} [4] and a broad band from 2500 to 3700 cm^{-1} including contributions from both O–H and C–H vibrational frequencies in formates and hydroxyl/water species. As catalyst deactivation proceeds in time, the carbonyl peak at 2117 cm^{-1} gradually reduces in intensity and shifts to 2104 cm^{-1}, reaching a steady intensity and position around 3.92 h. The decrease in carbonyl concentration is not resultant from catalyst reduction or reconstruction; DRIFTS experiments during catalyst reduction by CO show a dramatic increase in CO coverage as the catalyst is reduced. Also the catalyst is found to remain fully oxidized under the deactivation study conditions as evidenced by the lack of O_2 dependence on CO and H_2 oxidation rates (Section 3.6). The broad band at 2500–3700 cm^{-1}increases in intensity concurrently with the decrease in carbonyl peak intensity during deactivation. Changes in peak areas with time are shown in Fig. 13. Carbonate and Cu^+ carbonyl areas are represented by the integration of the stand-alone peaks at ~1026 and ~2110 cm^{-1}, respectively. The hydroxyl/water region is represented by the integration of the entire band from the abrupt rise around 3700 cm^{-1} to the area which flattens out around 2500 cm^{-1}. The carbonyl band in the current work is observed to decay with time much like the CO oxidation rate decays with time (Fig. 6). Thus, the carbonyl peak at ~2110 cm^{-1} correlates to CO oxidation rates and is expectedly resultant from CO adsorbed adjacent to active redox sites. In the event that adsorbed CO is the active intermediate to CO

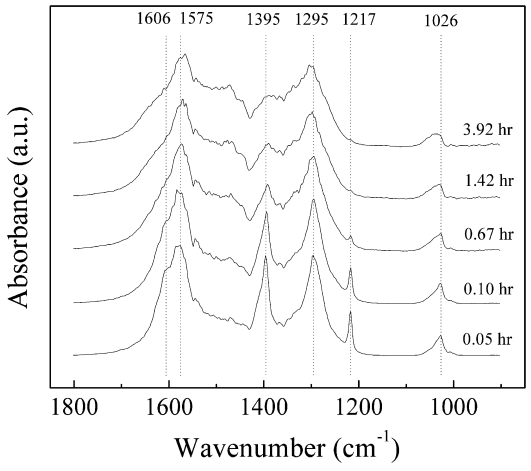

Fig. 11. Time evolution of carbonate/formate bands during $CuCeO_x$–UG 4.0 deactivation in 25% H_2, 1% CO, 3% O_2, balance He at 333 K. Catalyst pretreated in 10% O_2 balance He at 773 K.

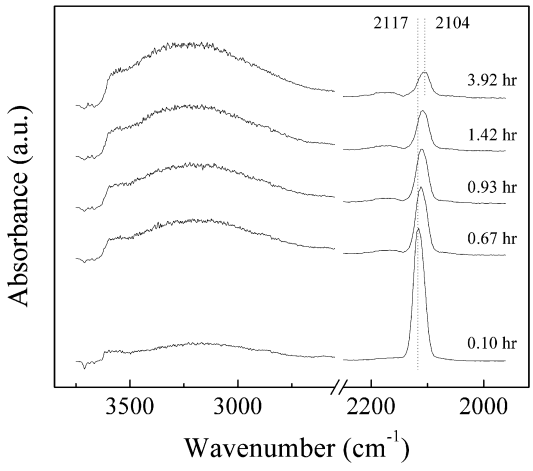

Fig. 12. Time evolution of carbonyl and hydroxyl bands during deactivation of $CuCeO_x$–UG 4.0 in 25% H_2, 1% CO, 3% O_2, balance He at 333 K. Catalyst pretreated in 10% O_2 balance He at 773 K.

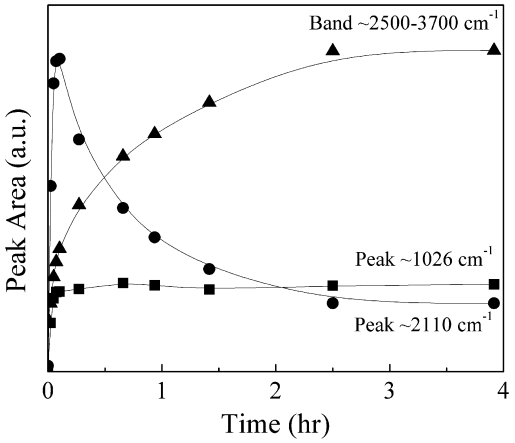

Fig. 13. Integrated DRIFTS peak areas as a function of deactivation time for three representative bands. Bands at 1026, 2110 and 2500–3700 cm^{-1} are representative of carbonates (■), carbonyl (●) and hydroxyl (▲) species, respectively. Reaction conditions: 50% H_2, 1% CO, 3% O_2, balance He. $CuCeO_x$–UG 4.0 catalyst pretreated in 10% O_2 balance He at 773 K.

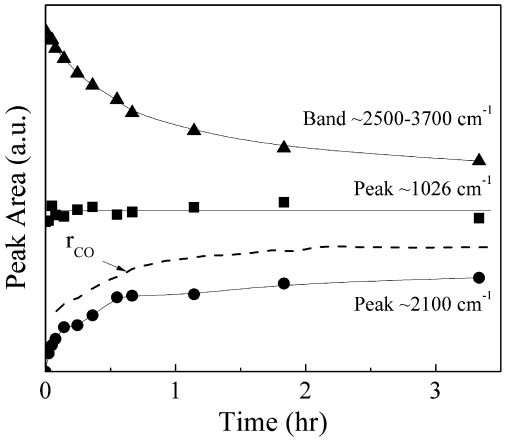

Fig. 15. Integrated DRIFTS peak areas as a function of time for three representative bands. Bands at 1026, 2110 and 2500–3700 cm^{-1} represent carbonates (■), carbonyl (●) and hydroxyl (▲) species, respectively. Dotted line represents CO oxidation rate measured in a separate experiment under the same conditions. Reaction conditions: 50% H_2, 1% CO, 3% O_2, balance He. $CuCeO_x$–UG 4.0 catalyst exposed to ambient conditions prior to reaction.

oxidation, it is expected that reaction rates should be proportional to adsorbed CO concentration. It follows that the dependence of adsorbed CO concentration must have the same dependence on gas phase CO concentration as the rate. Fig. 14 shows the dependence of the carbonyl peak area on the gas phase CO concentration. The measured order is 0.79, which is remarkably close to the dependence of the CO oxidation rate on CO concentration (order of 0.68, presented later in Fig. 18). Thus the CO oxidation rate is directly proportional to the carbonyl concentration. Previous work on a series of CuO_x–CeO_2 catalysts for selective oxidation of CO in H_2 related the carbonyl peak at 2120–2110 cm^{-1} to CO adsorbed on Cu^+ specifically and claimed that the intensity of this band is directly related to the CO oxidation rate [4], in agreement with this work. Furthermore, it is observed that the carbonate species saturate quickly (within 0.05 h) while the band associated with hydroxyl/water species grows slowly over the deactivation period, suggesting that the hydration of the surface (as opposed to carbonate formation) is a primary cause of catalyst deactivation.

To closer examine the effect of hydration on catalyst activity and deactivation, a time resolved DRIFTS study was conducted over a catalyst with an initially fully hydrated surface (no thermal pretreatment prior to reaction). Fig. 15 shows the time evolution of Cu^+ carbonyl, carbonate and hydroxyl species. The carbonate species are initially at the same concentration as in the deactivation experiment described in Fig. 13 and do not change with time. However, surface hydration reduces with time and the Cu^+ carbonyl peak increases with time, tending toward the same steady-state established at the end of deactivation. The CO oxidation rate also increases over this time period (measured during a separate experiment, shown in Fig. 15), corroborating the correlation between the carbonyl band at ~2110 cm^{-1} and the concentration of adsorbed CO on active sites.

The decrease of adsorbed CO in Fig. 13 correlates with the increase in the band from 2500 to 3700 cm^{-1} (increase in surface hydration). As the carbonyl peak decreases with increasing surface hydration, it shifts gradually to lower wavenumber (2117–2104 cm^{-1}). Fig. 16 shows the dependence of the carbonyl peak position on the hydroxyl/water band area, and a clear linear trend holds for both initially hydrated and initially dehydrated surfaces. Because the CO coverage is also changing during this experiment, the carbonyl peak was monitored during experiments in changing CO pressures (only CO coverage changes). The carbonyl peak position is constant (at 2104 cm^{-1}) upon changing CO pressures (0.5–4%) after deactivation, suggesting that the binding of CO is not coverage dependent at this range of coverage. Therefore, the linear correlation between carbonyl peak position and hydroxyl band area is not coincidental, nor is it convoluted by the changing carbonyl coverage. The red shift in the carbonyl peak indicates the

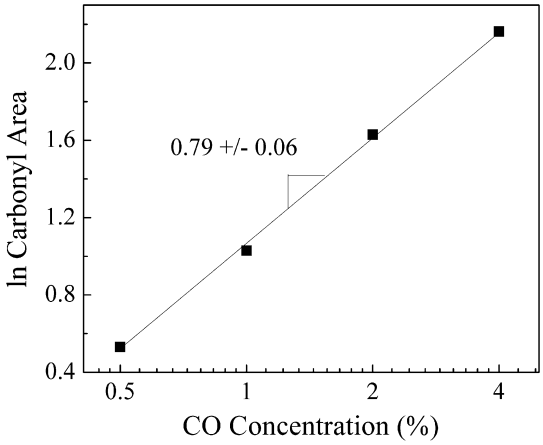

Fig. 14. Log–log plot of Cu^+ carbonyl area dependence on CO concentration on $CuCeO_x$–UG 4.0.

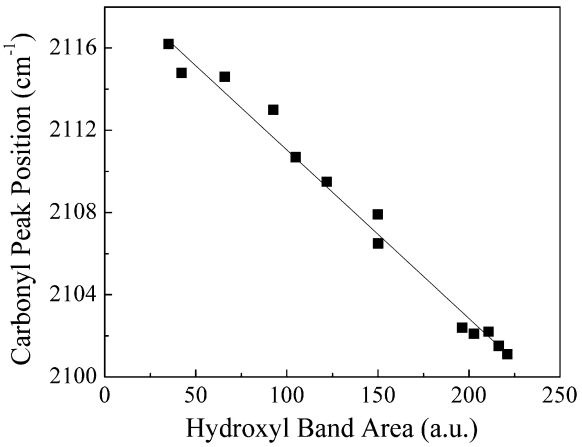

Fig. 16. Carbonyl peak position as a function of integrated hydroxyl band area.

C–O bond is weakened, suggesting that the CO binding to the catalyst has strengthened. This red-shift is most likely caused by the hydroxylation of oxygen sites adjacent to adsorption sites. An increase in surface hydroxylation will likely be accompanied by higher concentrations of molecular H_2O on adsorption sites, which can displace some of the adsorbed CO, as has been observed in other work [31]. This increase of adsorbed water explains why CO coverage can decrease despite an increase in CO binding energy. The change in CO binding energy with modification of adjacent oxygen sites presents an interesting opportunity to potentially tune the competitive adsorption properties as well as the CO oxidation rates of CuO_x–CeO_2 catalysts by titration of hydroxyl sites with alkali metals, seen elsewhere as a measure to prevent hydrogen spillover [32].

$$[L] = [M] + [CO{-}M] + [H{-}M] + [\,CO_2{-}M] + [H_2O{-}M] \tag{11}$$

$$[O^*]_T = [O^*] + [O^*{-}H] + [\square] \tag{12}$$

$$r_{CO_2} = \frac{k_{CO_2} K_{O_2}^{1/2} K_{CO}[CO][O_2]^{1/2}}{\left(1 + K_{CO}[CO] + K_{CO_2}[CO_2] + K_{H_2}^{1/2}[H_2]^{1/2} + K_{H_2O}[H_2O]\right)\left[1 + \left(1 + K_{OH}K_{H_2}^{1/2}[H_2]^{1/2}\right)K_{O_2}^{1/2}[O_2]^{1/2}\right]} \tag{13}$$

$$r_{H_2O} = \frac{k_{H_2O} K_{OH} K_{O_2}^{1/2} K_{H_2}[H_2][O_2]^{1/2}}{\left(1 + K_{CO}[CO] + K_{CO_2}[CO_2] + K_{H_2}^{1/2}[H_2]^{1/2} + K_{H_2O}[H_2O]\right)\left[1 + \left(1 + K_{OH}K_{H_2}^{1/2}[H_2]^{1/2}\right)K_{O_2}^{1/2}[O_2]^{1/2}\right]} \tag{14}$$

3.5. Mechanism formulation

A rigorous mechanism for competitive CO and H_2 oxidation is proposed and compared to kinetic measurements to provide insight into catalyst performance (activity and selectivity). CO oxidation selectivity is considerably higher than that calculated from independent CO and H_2 oxidation rates [16], suggesting that the presence of CO suppresses H_2 oxidation. Thus, competitive adsorption between CO and H_2 is proposed to be the initial step in the oxidation mechanism (Eqs. (3) and (6)). The full mechanism for CO and H_2 oxidation is written below where M represents an adsorption site, O^* represents a lattice oxygen and □ represents a lattice vacancy.

$CO + M \leftrightarrow CO{-}M$	K_{CO}	(3)
$CO{-}M + O^* \rightarrow CO_2{-}M + \square$	k_{CO_2}	(4)
$CO_2{-}M \leftrightarrow CO_2 + M$	$K_{CO_2}^{-1}$	(5)
$H_2 + 2M \leftrightarrow 2H{-}M$	K_{H_2}	(6)
$H{-}M + O^* \leftrightarrow O^*{-}H + M$	K_{OH}	(7)
$O^*{-}H + M{-}H \rightarrow H_2O{-}M + \square$	k_{H_2O}	(8)
$H_2O{-}M \leftrightarrow H_2O + M$	$K_{H_2O}^{-1}$	(9)
$O_2 + 2\square \leftrightarrow 2O^*$	K_{O_2}	(10)

From anaerobic titrations, it is concluded that the rate-determining step for both CO oxidation and H_2 oxidation must contain exactly one lattice oxygen atom. DRIFTS experiments show that the rate is first order in linearly adsorbed CO. The above-mentioned Eq. (4) is proposed from these observations. Eq. (8) is the reaction of an adsorbed H with a hydroxyl group. This is proposed because H_2 anaerobic titrations suggest that the step must involve both dissociated H_2 and a lattice oxygen. Products are proposed to be in adsorption equilibrium (Eqs. (5) and (9)) due to previous reports on CO_2 and H_2O rate inhibition, as well as neither product having a noticeable effect on the selectivity [2]. Eq. (7) is simply H-spillover to create hydroxyl species, which is a well-documented process on metal oxides [32]. Finally, Eq. (10) is the reoxidation of the active oxygen site by gas phase oxygen. The kinetics of metal oxide reoxidation are discussed elsewhere for VO_x systems [33]. Also, in this study, the precise steps of lattice reoxidation are considered kinetically irrelevant, as is demonstrated by a lack of CO and H_2 oxidation rate dependence on O_2 pressures (Section 3.6).

3.6. Reaction rate modeling

The above-mentioned mechanism can be used to formulate a reaction rate model for both CO and H_2 oxidation, shown below in Eqs. (13) and (14). These are rigorous rate expressions, obtained by considering two site balances (Eqs. (11) and (12)), one for the adsorption site (M) including all involved surface species, and one for the lattice oxygen site (O^*) including O^*, O^*–H and □.

A model for the reaction selectivity vs. CO and H_2 concentrations can be obtained by computing the ratio (R) of CO and H_2 reaction rates, as shown below in Eqs. (15) and (16). This model is conservative, makes no additional assumptions and provides a single lumped parameter (K') fit. Fig. 17 shows the reaction selectivity as a function of both CO and H_2 concentrations, as well as the fitted model. With only one parameter, the model provides a good qualitative fit of the experimental data, supporting the validity of the proposed mechanism. It should be emphasized, however, that the parameter K' has no physical significance and that the model is simply indicating the same trends as seen in the data. This qualitative agreement only precludes mechanisms which would result in substantially different kinetics, such as CO inhibited CO oxidation.

$$R = r_{H_2O}/r_{CO_2} = k_{H_2O} K_{OH} K_{H_2}[H_2]/k_{CO_2} K_{CO}[CO] = K'[\,H_2]/[CO] \tag{15}$$

$$1/S_{CO_2} = (r_{CO_2} + r_{H_2O})/r_{CO_2} = 1 + R \tag{16}$$

The rate expressions (Eqs. (13) and (14)) can alternatively be simplified by making a few assumptions in order to predict what the reaction order should be with respect to all reactants and products. For example, if the reoxidation step occurs very readily (i.e. $\square \rightarrow 0$), and CO concentration approaches very low levels, the CO order for CO oxidation approaches 1. Conversely, if the CO concentration reaches very high levels and CO–M is the most abundant surface intermediate, the CO order of CO oxidation approaches 0. The same logic can be applied for all the participating species, and Table 6 contains all the expected order ranges. Fig. 18 shows the CO and H_2 oxidation reaction rate dependence on CO, H_2 and O_2 over $CuCeO_x$–UG 4.0 and the resultant reaction orders. All reaction orders measured are within the bounds expected from the model. Therefore, the data are consistent with those of both the proposed and simplified models.

The kinetic results and proposed mechanism show that both the oxidation of CO and H_2 over CuO_x–CeO_2 catalysts must occur by a Mars and van Krevelen pathway utilizing catalyst redox cycles. Also, two main factors contributing to the high selectivity of these catalysts are preferential adsorption of CO and inhibition of H_2 dissociation by oxidized sites, yielding two useful parameters for PROX catalyst design. An optimally selective catalyst would

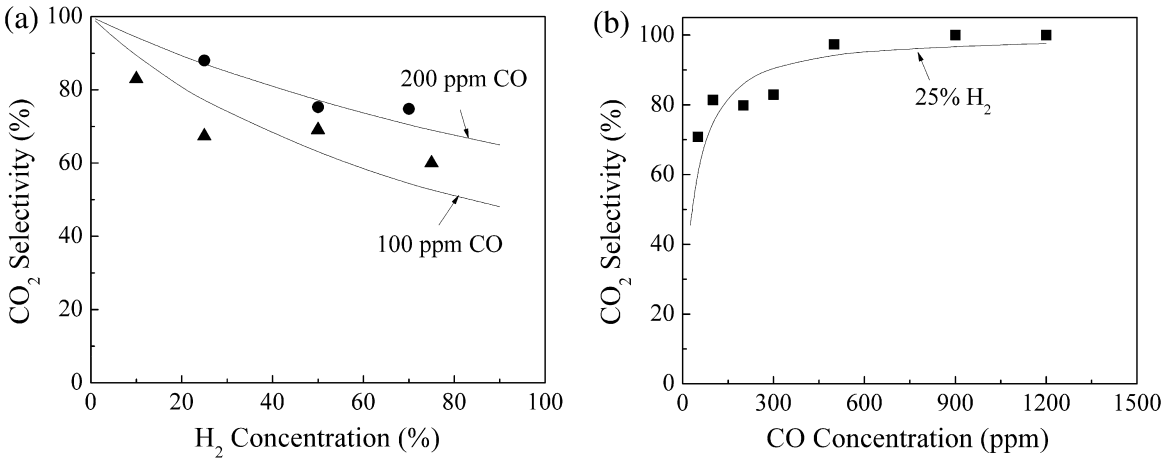

Fig. 17. Lumped parameter fit ($K' = 1.1 \times 10^{-4}$) of selectivity data vs.: (a) H_2 pressure for (▲) 100 ppm CO and (●) 200 ppm CO, (b) CO pressure for (■) 25% H_2. Oxygen concentration for all experiments is stoichiometric with respect to CO. CO conversion for all data is <10%. Model (Eq. 15) is shown by the solid lines.

Table 6
List of all possible reaction order ranges for both CO and H_2 oxidation.

Component	Possible reaction order ranges derived from the proposed mechanism	
	CO oxidation	H_2 oxidation
CO	0 to 1	−1 to 0
CO_2	−1 to 0	−1 to 0
H_2	−1 to 0	0 to 1
H_2O	−1 to 0	−1 to 0
O_2	0	0

therefore contain adsorption sites which prefer CO to H_2 (Cu^+ acts as a good site in this respect), and can remain oxidized under highly reducing conditions. As high CO oxidation rates are desirable, catalysts with high surface densities of adsorption sites are needed, since CO rates correlate directly to adsorbed CO. However, increased surface densities of adsorption sites must not be at the expense of active redox sites, thus a highly incorporated Cu–Ce mixed oxide (as opposed to supported CuO_x) with a high Cu concentration seems to be the optimal configuration providing high rates.

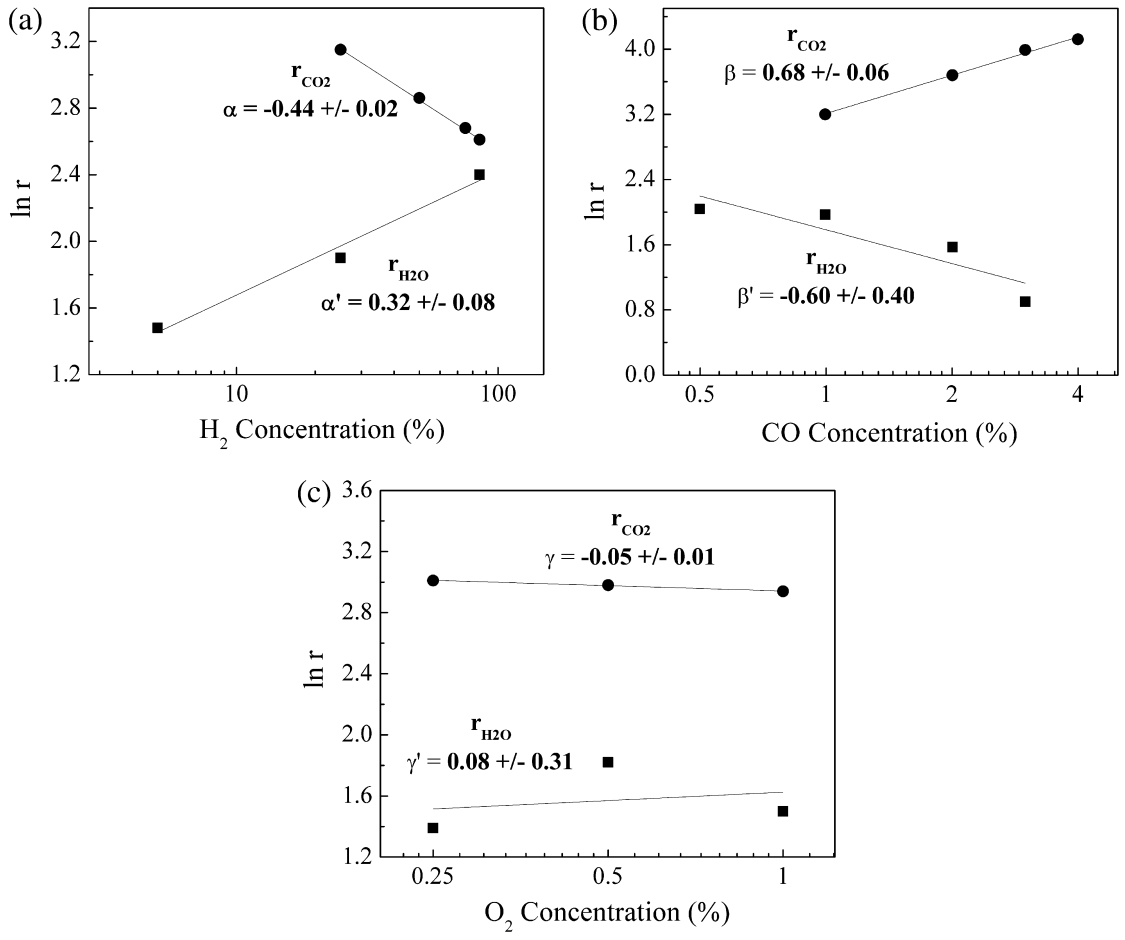

Fig. 18. CO and H_2 oxidation orders over $CuCeO_x$–UG 4.0 for (a) H_2, (b) CO and (c) O_2 where $r_{CO_2} = k[H_2]^{\alpha}[CO]^{\beta}[O_2]^{\gamma}$ and $r_{H_2O} = k'[H_2]^{\alpha'}[CO]^{\beta'}[O_2]^{\gamma'}$.

4. Conclusions

A detailed study of CO and H_2 oxidation over CuO_x–CeO_2 catalysts with variable Cu content and incorporation was performed with the following major conclusions:

- Both CO and H_2 oxidation pathways occur via a Mars and van Krevelen mechanism involving the reduction and oxidation of active oxygen sites. CO oxidation proceeds through linearly adsorbed CO on Cu^+ sites, while H_2 oxidation requires a dissociative adsorption step. The proposed mechanism-based kinetic model is in good agreement with the experimental data.
- Catalyst deactivation is directly related to the degree of surface hydration, likely due to blocking of sites by molecular water.
- Redox sites can be accurately quantified by the anaerobic titration technique (using either CO, H_2 or both), and an intrinsic rate can be measured that does not depend on copper loading or catalyst synthesis technique.
- The surface density of copper atoms directly relates to the surface density of active oxygen sites on the catalyst in the absence of highly crystalline CuO_x species, suggesting that the presence of active oxygen species in the form of Cu–O–Ce.
- The high selectivity of CuO_x–CeO_2 catalysts can be attributed to both preferential adsorption of CO on Cu^+ and a hindered H_2 dissociation on oxidized sites.

Acknowledgments

This work was funded by Purdue University and the Purdue Research Foundation. The authors acknowledge Dr. Dima Zemlyanov for XPS measurements and Ms. Rebecca Freeman for help with catalyst synthesis and FTIR characterization during a summer REU program at Purdue University (EEC #0552933).

References

[1] F. Marino, C. Descorme, D. Duprez, Applied Catalysis B: Environmental 58 (2005) 175.
[2] G. Avgouropoulos, T. Ioannides, H.K. Matralis, J. Batista, S. Hocevar, Catalysis Letters 73 (2001) 33.
[3] G. Avgouropoulos, T. Ioannides, Applied Catalysis B: Environmental 67 (2006) 1.
[4] D. Gamarra, C. Belver, M. Fernandez-Garcia, A. Martinez-Arias, Journal of American Chemical Society 129 (2007) 12064.
[5] D. Gamarra, G. Munuera, A.B. Hungria, M. Fernandez-Garcia, J.C. Conesa, P.A. Midgley, X.Q. Wang, J.C. Hanson, J.A. Rodriguez, A. Martinez-Arias, Journal of Physical Chemistry C 111 (2007) 11026.
[6] C.R. Jung, J. Han, S.W. Nam, T.-H. Lim, S.-A. Hong, H.-I. Lee, in: Catalysis Today Selections from the Presentations of the Third Asia-Pacific Congress on Catalysis, vol. 93–95, 2004, p. 183.
[7] Y. Liu, Q. Fu, M. Flytzani-Stephanopoulos, Catalysis Today 93–95 (2004) 241.
[8] C. Lamonier, A. Ponchel, A. D'Huysser, L. Jalowiecki-Duhamel, Catalysis Today 50 (1999) 247.
[9] G. Marban, A.B. Fuertes, Applied Catalysis B: Environmental 57 (2005) 43.
[10] A. Martinez-Arias, A.B. Hungria, M. Fernandez-Garcia, J.C. Conesa, G. Munuera, Journal of Physical Chemistry B 108 (2004) 17983.
[11] E. Moretti, M. Lenarda, L. Storaro, A. Talon, R. Frattini, S. Polizzi, E. Rodriguez-Castellon, A. Jimenez-Lopez, Applied Catalysis B: Environmental 72 (2007) 149.
[12] G. Sedmak, S. Hocevar, J. Levec, Journal of Catalysis 213 (2003) 135.
[13] W. Shan, Z. Feng, Z. Li, J. Zhang, W. Shen, C. Li, Journal of Catalysis 228 (2004) 206.
[14] X. Tang, B. Zhang, Y. Li, Y. Xu, Q. Xin, W. Shen, Applied Catalysis A: General 288 (2005) 116.
[15] W. Liu, M. Flytzani-Stephanopoulos, Journal of Catalysis 153 (1995) 317.
[16] C.S. Polster, C.D. Baertsch, Chemical Communications (2008) 4046.
[17] W. Liu, M. Flytzani-Stephanopoulos, Journal of Catalysis 153 (1995) 304.
[18] M.A. Vannice, Catalysis Today 123 (2007) 18.
[19] H. Nair, C.D. Baertsch, Journal of Catalysis 258 (2008) 1.
[20] J.W. Niemantsverdriet, Spectroscopy in Catalysis, Wiley-VCH, Weinheim, 2000.
[21] S. Zhou, Z. Yuan, S. Wang, International Journal of Hydrogen Energy 31 (2006) 924.
[22] P. Kubelka, F. Munk, Zeitschrift fur Physik 12 (1931) 593.
[23] A.G.-G. Varez, E. Jolly, J. Sanz, Journal of the European Ceramic Society 27 (2007) 3677.
[24] C.C. Ahn, O.L. Krivanek, The EELS Atlas, Pleasanton, CA, USA.
[25] O. Pozdnyakova, D. Teschner, A. Wootsch, J. Krohnert, B. Steinhauer, H. Sauer, L. Toth, F.C. Jentoft, A. Knop-Gericke, Z. Paal, R. Schlogl, Journal of Catalysis 237 (2006) 1.
[26] H.C. Yao, Y.F.Y. Yao, Journal of Catalysis 86 (1984) 254.
[27] A. Martínez-Arias, D. Gamarra, M. Fernández-García, A. Hornés, P. Bera, Z. Koppány, Z. Schay, Catalysis Today 143 (2009) 211.
[28] J.Y. Kim, J.A. Rodriguez, J.C. Hanson, A.I. Frenkel, P.L. Lee, Journal of the American Chemical Society 125 (2003) 10684.
[29] C. Li, Y. Sakata, T. Arai, K. Domen, K.-I. Maruya, T. Onishi, Journal of the Chemical Society, Faraday Transactions 85 (1989) 929.
[30] C. Binet, A. Badri, M. Boutonnet-Kizling, J.-C. Lavalley, Journal of the Chemical Society, Faraday Transactions 90 (1994) 1023.
[31] D. Gamarra, A. Martínez-Arias, Journal of Catalysis 263 (2009) 189.
[32] C. Pedrero, T. Waku, E. Iglesia, Journal of Catalysis 233 (2005) 242.
[33] B. Frank, R. Fortrie, C. Hess, R. Schlögl, R. Schomäcker, Applied Catalysis A: General 353 (2009) 288.
[34] M.L. Foo, Q. Huang, J.W. Lynn, W.-L. Lee, T. Klimczuk, I.S. Hagemann, N.P. Ong, R.J. Cava, Journal of Solid State Chemistry 179 (2006) 563.
[35] W.L. Bragg, Philosophical Magazine Series 6 (28) (1914) 255.